Experimental investigation of vortex-induced vibrations of a circular cylinder under rotary oscillations

Agathe Schmider, Franck Kerhervé, Laurent Cordier, Andreas Spohn, Nicolas Dellinger

EXPERIMENTAL INVESTIGATION OF VORTEX-INDUCED VIBRATIONS OF A CIRCULAR CYLINDER UNDER ROTARY OSCILLATIONS

Agathe Schmider, Franck Kerhervé, Laurent Cordier & Andreas Spohn
Institut Pprime, Université de Poitiers, CNRS, ISAE-ENSMA, Poitiers, France

Nicolas Dellinger
ICUBE, Université de Strasbourg, Strasbourg, France

ABSTRACT

A new experimental device to study vortex-induced vibrations (VIV) of a cylinder in a free-surface water channel is presented. The cylinder is elastically-mounted on an air-bearing platform and is free to oscillate in the cross-flow direction. Two DC motors are coupled to the oscillating mass and allow : (i) to simulate for positive or negative damping through forcing, (ii) to measure the position and speed of the cylinder, (iii) to force the cylinder into a rotative motion. The dynamical response of the system has a typical two or three branch response amplitude depending on the damping ratio. One case of intensification of VIV oscillations with rotary oscillations is detailled. Flow velocity surveys obtained with Particle Image Velocimetry (PIV) are reported to compare the different VIV wake modes.

1. INTRODUCTION

The study of the formation of vortex structures around a bluff body immersed in a flow has a long tradition in fluid mechanics. If this body has a natural resonance frequency or a certain flexibility of motion, a fluid-structure interaction phenomenon can arise. The more the frequency of the vortex shedding coincides with the natural frequency of the mechanical system, the greater the induced vibrations. The damage of engineering structures or the generation of noise in the presence of strong winds are direct consequences. This phenomenon, commonly called "vortex-induced vibrations" (VIV), is also at the origin of energy extraction test devices such as the one of the VIVACE project (**?**), which consists of an elastically mounted cylinder connected to a generator. While former studies focus on arrangements with constant viscous damping, the present study takes advantage of an oscillator with adjustable characteristics. At this end, the present experimental set-up allows to change damping as a function of oscillation amplitude. The device can be modelled as a damped mass-spring system, thus it is necessary to be able to adjust its mechanical parameters in a non-intrusive way (see **?**, for example). In this work, several mechanical parameters are controlled such as the damping or the forced rotation of the cylinder around its main axis. The damping is achieved by a DC motor, in a similar way to the system of **?**.

Early studies on VIV control focused on vibration reduction or suppression (**?**). For this purpose, cylinder rotation is often used (**?**). The numerical study of **?** at low Reynolds number shows that cylinder rotation can intensify the oscillations. Experimental studies on the influence of cylinder rotation on the amplitude of free oscillations are rare and very recent (**??**). The team from the Flair laboratory at Monash University, accustomed to experiments on VIVs (**????**), has observed several cases of alternating rotations in which the oscillations are strongly enhanced (**?**). The experimental setup was dimensioned to achieve similar values of rotation rates in order to achieve efficient forcing.

2. EXPERIMENTAL DEVICE

2.1. Water channel

The experiments presented are conducted in the home-made circulating water channel Hydra III at Institut Pprime (Poitiers, France). The overall set-up is schematically represented in Figure **??**. The power section relies on an axial pump located under the water channel. The flow is pumped through a recirculating pipe and transmitted to a settling chamber made in composite through a vertical circular inlet diffuser. The water flow then passes through a honeycomb covered by foam and followed with a series of fine screens. The settling chamber ends with a convergent made in composite so that the flow enters the test section with a turbulence intensity of less than 5%. The test section is 2.1m long, 0.51 m wide and 0.51 m height and is made of glass windows to allow optical access from both sides as well from below and through the main flow direction. The water depth in the test section is fixed to 0.33 m. The freestream

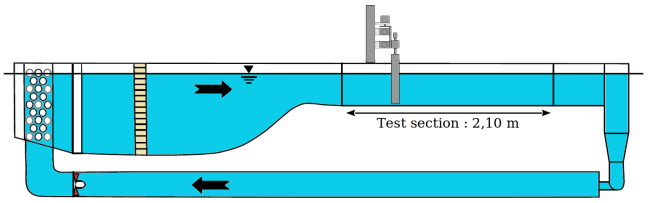

Figure 1. Simplified diagram of the water channel and position of the experimental arrangement

velocity ranges from 5 to 45 $\mathrm{cm\,s^{-1}}$. The flow uniformity all along the test section was checked thanks to two-dimensional two-component (2D-2C) Particle Image Velocimetry (PIV) measurements performed in different planes not reported here for conciseness.

2.2. Oscillating device

The oscillating device is shown in Figure **??**. A circular hollow cylinder made in aluminium of diameter $D = 50$ mm, $L = 0.4$ m long and $e = 1.8$ mm thick is vertically immersed in the water channel. The blockage ratio due to the presence of the cylinder in the test section is 10%. A gap between the cylinder end and the channel floor is set to 2 mm. The cylinder is mounted on a platform made in aluminium which supports three OAV air bearings alimented by pressurised air at 4 bars. These air bearings guide the mobile platform with negligible mechanical friction in the crossflow direction along two shafts made in high precision stainless steel of 20 ± 0.02 mm diameter. The platform is elastically-mounted with a pair of linear springs (LeeSpings LE014B13S) mounted in parallel on each side. The resulting total stiffness coefficient is $k = 0.022$ $\mathrm{N\,mm^{-1}}$. A low inertia 24V DC servo motor with a dual track encoder is coupled to the oscillating platform with a rack pinion mechanism. The pinion radius is $r_p = 25$ mm. Such arrangement results in additional dry friction due to the mechanical coupling. However, the motivations for such arrangement is threefold. First, it allows a robust and accurate solution to measure in real-time the position $y(t)$ and velocity $\dot{y}(t)$ of the cylinder. Secondly, it allows to have a metric of the energy which can be harvested from the oscillating system by measuring on-line the generated current. Finally, the motor can be used to apply an arbitrary displacement of the cylinder or to simulate positive or negative damping effect such as to compensate for the additional source of friction for example.

With this arrangement, the cylinder can operate displacement over $\pm 2D$ in the cross-flow direction with minimal damping. The overall oscillating mass is $m = 2.486$ kg which results in a mass ratio $m^* = m/m_A = 3.8$ with m_A the displaced mass of water.

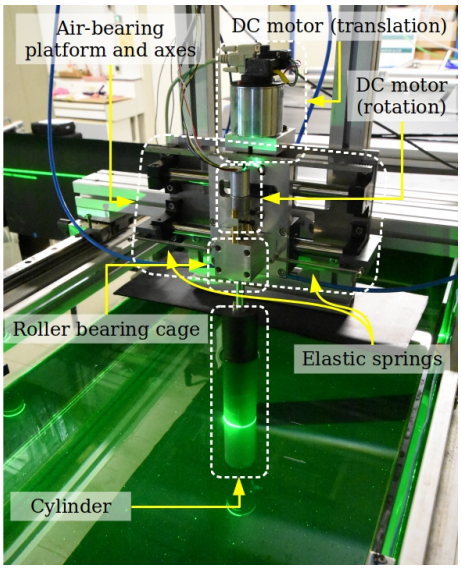

Figure 2. Experimental VIV device.

2.3. Rotating device

The cylinder is fixed on an aluminium shaft guided by two ball bearings mounted in an aluminum cage. It is driven in rotation by a second, smaller (6 volt) DC motor to limit the mass of the moving parts. Three models of motors can be used to change the maximum speed reached by the motor (between 100 and 300 rpm). This motor is controlled by a pulse width modulation (PWM) signal from an Arduino Due interfacing the motor with the rest of the acquisition system presented in the section **??**. The choice for this application of a DC motor comes from the ease of implementation of a PWM command to control the torque. The motor is also equipped with an encoder with 11 pulses per revolution which allows to have a feedback on the angular position of the cylinder and to calibrate each motor. The rotation command used is of the form $\Omega(t) = \Omega_0 sin(2\pi f_r t)$, which gives an alternating rotation of the cylinder with a maximum rotation speed Ω_0. In order to compare the obtained results with previous research works, the dimensionless parameter $\alpha = \Omega_0 D/2U_\infty$ defines the reduced rotation speed. One objective of this work is to verify if the oscillations of the cylinder in the VIV regime can be increased by rotary oscillation of the cylinder. Simultaneous measurements of cylinder displacement, cylinder rotation speed and velocity fields by 2D2C PIV have been performed.

2.4. Instrumentation

As mentioned above, the DC motor is directly used to measure both the displacement $y(t)$ and velocity $\dot{y}(t)$ of the cylinder. The in-built encoder provides TTL

output signals with 500 pulses per revolution and enables to measure position and speed accurately. Both signals are sampled at 500 Hz with one of the acquisition NI PXIe-6356 I/O cards used. A planar two-component particle image velocimetry (PIV) system was used for velocity surveys in the near-wake of the cylinder. The PIV system includes a Nano L 50-50 PIV laser from Litron Ltd (wavelength 532 nm) of 50 mJ per pulse and a Dantec SpeedSence 1040 camera with a resolution of 2320×1726 pixels oriented towards the wake region through a mirror inclined at 45° installed underneath the water channel. The measurement plane is located at mid-heigh of the water channel and covers a region of $8D \times 9D$ including the cylinder. The laser sheet is 1 mm thick. Polyamide particles of 50 µm diameter are used for flow seeding. The instantaneous vector fields are obtained using the acquisition software Davis 10 from Lavision. A dynamic mask following the cylinder displacement is used to avoid spurious correlations. The location of the mask for a given pair of images is set by the simultaneous measurements of the cylinder location. A conventional direct cross-correlation process including multipass windows (from 64×64 to 32×32) with 50% overlapping is used, leading to a final vector spacing of $0.09D$ in both directions. A bad-vector-replacement step is provided using a 5×5 median interpolation method. Finally, for a given PIV run, 3000 snapshots sampled at $f_{\mathrm{PIV}} = 15$ Hz, covering approximately 50 oscillations of the cylinder, are acquired.

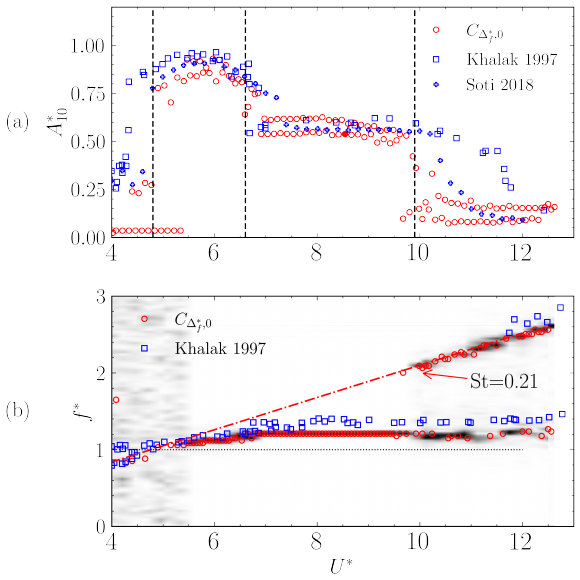

Figure 3. Study of the "frictionless" configuration and without rotation $C_{\Delta^*_f,0}$. (a) Amplitude response A^*_{10} as a function of reduced velocity U^* and comparison with the results of ? and ?. $A^*_{10} = A_{10}/D$ where A_{10} is the average amplitude calculated over the responses whose maximum amplitude is among the highest 10%. (b) Frequency response as a function of reduced speed U^* and comparison with the results of ?.

3. RESULTS

3.1. Validation of the experimental device

In this section, the experimental system in its "frictionless" and rotation-free configuration, denoted $C_{\Delta^*_f,0}$, is validated by comparison with different experimental works previously performed. To do so, we consider equivalent values of $m^*\zeta$ (??) where ζ, the structural damping ratio, is approximately equal to 0.020. The amplitude response is shown in Figure ??(a) as a function of reduced velocity $U^* = U_\infty/f_{\mathrm{nw}}D$ where f_{nw} is the natural frequency of the system. The non-rotating configuration $C_{\Delta^*_f,0}$ exhibits a typical three-branch response : (i) an initial branch ($U^* \leq 4.8$) with low oscillation amplitude, (ii) an upper branch located in the range $4.8 \leq U^* \leq 6.6$ where the cylinder experiences the largest oscillation amplitudes (approximately $0.8D$), and (iii) a lower branch on the range $6.6 \leq U^* \leq 9.5$ where the amplitude is limited to about $0.55D$. The so-called desynchronized region obtained for $U^* > 9.5$ is characterized by negligible oscillations. The normalized frequency response is shown in Figure ??(b). The power spectral density (PSD) of the displacement was evaluated for a given value of the reduced velocity to extract the frequency of the largest energy peak. Along the initial branch, the frequency response of the cylinder f_{VIV} is equal to the vortex release frequency f_{sh}, measured as $0.21U_\infty/D$. Moving to the lower branch, the cylinder frequency increases slightly to lock approximately on f_{nw}. This is illustrated by the dashed horizontal line obtained for $f^* = f_{\mathrm{VIV}}/f_{\mathrm{nw}} = 1$. The frequency response along the upper and lower branches is said to be synchronized until it reaches the desynchronized region. In the latter, the frequency response reaches the vortex release frequency again, while the vibrational response may also undergo low amplitude modulation at the natural frequency. In this region, the PSDs effectively exhibit two frequency peaks. These results, consistent with those reported in the literature for comparable values of structural damping ratio $m^*\zeta$ (??), suggest that the $C_{\Delta^*_f,0}$ configuration covers the expected parameter range. This configuration without rotation will be considered the reference case in the following.

3.2. Rotary oscillations

The hydrodynamic force due to the injection of circulation by a rotating cylinder in a flow has been known as the "Magnus effect" (**?**). More precisely the Magnus force is propotional to the rotation speed of the cylinder Ω_0 and the flow velocity U_∞.

3.2.1. Lock-in cases identification

The cylinder is here free to oscillate in the cross-flow direction while being forced into a rotative motion such that $\Omega(t) = \Omega_0 sin(2\pi f_r t)$. To identify cases where VIV may be increased by rotary oscillation, the parameter space (f_r^*, α) is explored at a constant reduced velocity $U^* = 8.4$. This case corresponds to the middle of the lower branch where oscillation amplitudes are limited ($A_{10}^* \approx 0.55$). The range of the parameter space was limited by the DC motors capacities and by the length of the air-bearings shafts which were designed for oscillation amplitudes $A^* \leq 2D$. The ampliture contours presented in Figure **??** show two zones of VIV intensification by rotary oscillation. (i) For $f_r^* \approx 1$ the cylinder observes high amplitude oscillations comparable to upper branch cases. The frequency around which these high amplitudes occur widens as α is increased. When the forcing frequency is further increased, the oscillation amplitude drastically decreases, even stops for some high rotation speed cases until the second zone is reached. (ii) For frequencies $f_r^* \approx 2.5$ the oscillation amplitude reaches levels slighly higher than the reference case without rotation. These two VIV amplification cases have been observed by **?** in their experimental work. The following part of the work presented here will focus on the most important case of VIV amplification for $f_r^* = 1$ and $\alpha = 0.9$.

3.2.2. VIV intensification by rotary oscillations

Here the cylinder is forced into a rotary oscillation of the form $\Omega(t) = \Omega_0 sin(2\pi f_r t)$. To obtain the amplitude response visible on the Figure **??**, upstream velocity is modified by steps of 1 $\mathrm{cm\,s^{-1}}$, first increasing, then decreasing. The data from the two motors are recorded at a frequency of 500 Hz. The shape of the amplitude response of the cylinder in alternating rotation is different from the reference obtained previously. Instead, we observe a decrease in the oscillation amplitudes for reduced speeds $U^* < 7$. Then, as the reference case shifts to the lower branch, the oscillation amplitudes continue to increase until they reach a plateau for $U^* = 8$. Our measurements are very consistent with those obtained experimentally by **?**, with strong deviations for relative velocity values U^* higher than 7.5. This result can be explained by the use of a DC motor with torque control which induces a dispersion in the peak rotation speeds.

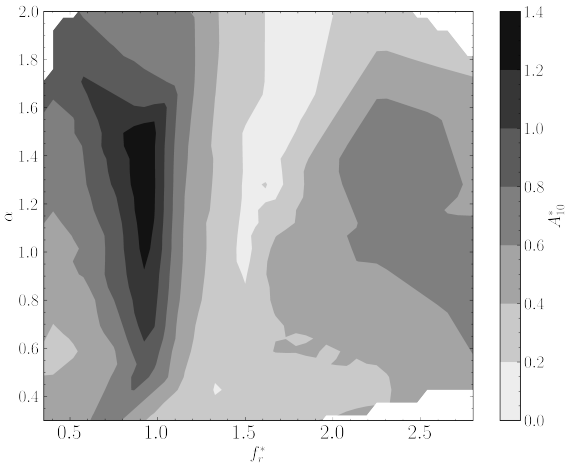

Figure 4. Amplitude response A_{10}^* contours in the (f_r^*, α) parameter space for reduced velocity $U^* = 8.4$.

The oscillation amplitudes are greatly increased by the use of rotary oscillations. In the section **??**, the time of establishment of the Magnus force will be investigated to try and understand why.

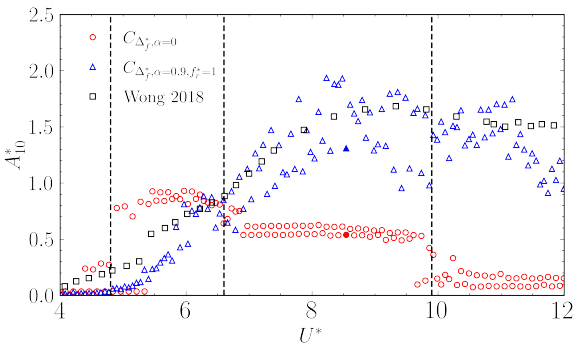

*Figure 5. Amplitude response A_{10}^* as a function of reduced velocity U^* for the configuration without rotation (red circles) and with alternating rotation (blue triangles). Comparaison with **?** obtained with $\alpha = 1$ and $f_r^* = 1$ (black squares).*

3.2.3. Wake patterns behind a cylinder under simultaneous VIV and rotary oscillations

A synchronized acquisition of the velocity fields and the linear and angular positions of the cylinder is performed by the method presented in section **??**. On the Figure **??**, the voticity fields are compared with the case without rotation. Since the frequency response

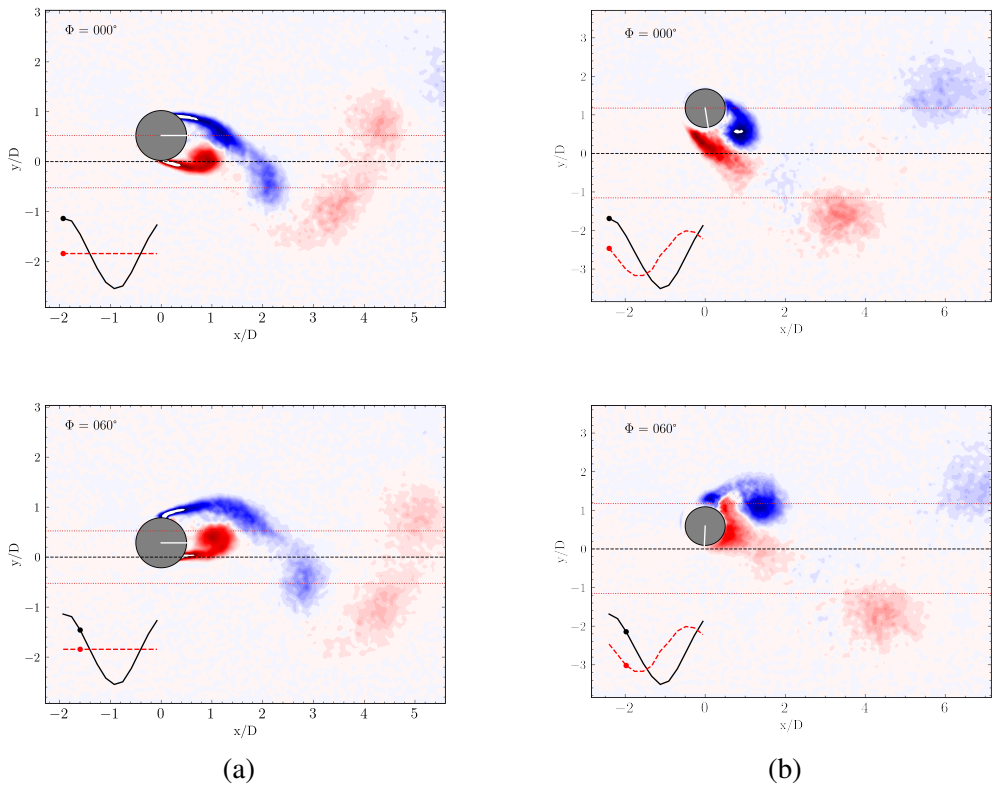

(a) (b)

Figure 6. Sequences of phase-averaged vorticity snapshots for $U^* = 8.4$(a) no rotation ($C_{\Delta^*_f,0}$) , (b) rotary oscillations ($\alpha = 0.89$, $f^*_r = f_r/f_{VIV} = 1$). Graphs in the bottom left corner show the linear position (black line) and the angular velocity (red dashed line) of the cylinder.

of the oscillating cylinder is quasi-periodic (see section **??**), the formation of vortices in the cylinder wake is characterized here by a phase-averaged representation. A slight time dependence ($\pm 6\%$) of the oscillation frequency is observed (not reported here for conscisness). In what follows, the phase-averaged velocity is defined according to the phase $\phi_i \in [0, 360°]$ ($i = 0 \ldots, N_\phi$) of the dominant oscillation period, where N_ϕ denotes the total number of phases considered. Due to the slight variation in time of the period of the dominant oscillation, the relative temporal position of a given phase also changes slightly between two consecutive maxima. Therefore, the instants corresponding to a given phase ϕ_i are first evaluated independently for each oscillation period. For a given phase instant ϕ_i, the PIV fields corresponding to $[\phi_i \pm \Delta\phi]$ are then collected and averaged to form the phase-averaged velocity field $\overline{\boldsymbol{u_i}}$. The latter thus describes, on average, the velocity field obtained in the wake of the cylinder at a given phase instant of the VIV process. In the following, we consider $N_\phi = 12$ and $\Delta\phi = 10°$. The latter value has been found to present a good compromise between the phase localization and the number of PIV snapshots collected for a satisfactory statistical convergence. The obtained two-dimensional phase-averaged velocity field is then used to compute a phase-averaged rotational field from which wake regimes can be identified.

Sequences of phase-averaged vorticity fields are shown on the Figure **??** for the reduced velocity value U^* given by the solid symbols on the Figure **??**. In the sequences reported on the Figure **??**, the cylinder moves from one of its extreme positions to the other. The Figure **??**(a) refers to a VIV regime in the middle of the lower branch ($U^* = 8.5$), without rotation. The wake consists of two vortices of opposite sign that break off per half cycle of oscillation forming pairs. This pattern is commonly called $2P$ (**??**). The two vortices released per oscillation cycle have similar intensity and thus persist downstream. We observe a double row of vortex pairs with a spacing in the current direction of about $1.5D$ and a transverse spacing of about $2D$. While on the lower branch, the cylinder undergoes oscillation with a smaller amplitude than in the upper branch, it should be noted that the first vortex released in the oscillation cycle is pushed further away from the centerline due to

the equivalent action of the second vortex. The Figure **??**(b) refers to the same reduced velocity value as before, but for an alternating rotation defined by $\alpha = 0.89$ and $f_r^* = f_r/f_{\mathrm{VIV}} = 1$. In the far wake, we observe two rows of counter-rotating vortices with a lateral spacing of about $3.5D$ and a spacing in the current direction of about $4D$. Unlike the non-rotating case, the vortices do not appear to remain in pairs, although a second, weaker vortex appears to break away upon release. Moreover, the connection between two vortices of the same direction of rotation, observed in the reference case, is no longer present in the case with rotation, certainly due to the rapid dissipation of the second vortex. The wake is twice as wide as in the reference case, consistent with the increase in the amplitude of the oscillations.

3.2.4. Circulation around the cylinder under transitional rotation

To better understand how the rotary oscillation can increase VIV oscillations, the transitional regime of the Magnus effect was experimentally investigated. For this purpose, velocity field measurements were performed during the rotation of the cylinder, this one being initially fixed in a constant velocity flow U_∞. For the acquisition of the velocity fields, the configuration presented in section **??** is used with a second laser upstream of the cylinder in order to have the velocity field around the whole circumference of the cylinder. The synchronization of the two lasers limits the acquisition frequency to $f_{\mathrm{PIV}} = 17$ Hz. The field of view is about $3.5D \times 3.5D$, centered on the cylinder. The spatial resolution of the vector field is $\Delta x = \Delta y = 0.051D$.

The circulation $\Gamma = \oint_C \boldsymbol{V} \cdot \boldsymbol{dl}$ is computed on the circle of diameter $D + \delta D$, varying δD on the interval $[\Delta x, 10\Delta x]$. The mean velocity fields are calculated for $\alpha = 0$ and for $\alpha = 0.82$. The Figure **??** shows that without rotation of the cylinder the wake is symmetrical (left) whereas an asymmetry appears when the cylinder is rotating (right). This observation is confirmed by the calculation of the circulation (see Figure **??** below). When the cylinder is rotated, the average circulation is strongly increased. It goes from a value close to zero, consistent with the evolution of the lift coefficient of a fixed cylinder (**?**), to a higher average value. The Γ circulation varies before and after the cylinder is rotated at frequency f_{sh}. The time of establishment of the Magnus force is estimated using a sliding average of Γ. We thus determine a characteristic time $\tau_{0.9}$ which corresponds to the time needed for the sliding average of Γ (blue continuous curve in the Figure **??**) to reach 90% of its average value when the cylinder is rotating. We obtain $\tau_{0.9}/f_{\mathrm{sh}} \approx 1$. The phenomenon seems to have the same characteristic time as the vortex shedding. These two phenomena could thus dynamically compete, or collaborate.

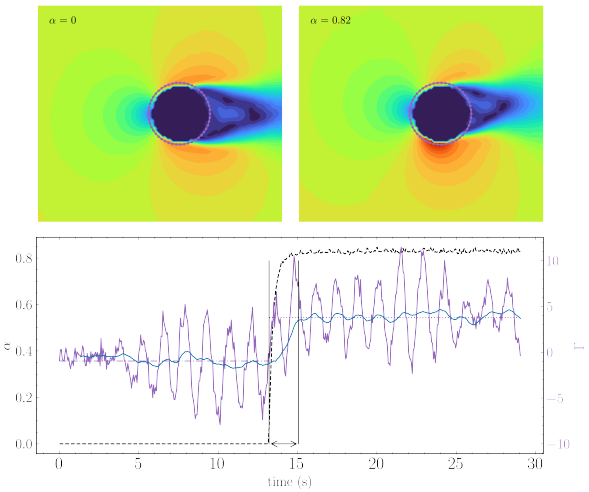

Figure 7. Top : Mean velocity norm $\|\overline{\boldsymbol{V}}\|$ without rotation (left) and with rotation (right). Bottom : Time series of the cylinder rotation speed α (black dashed line) and of the circulation Γ (purple) computed over the circular closed contour shown in purple on the mean velocity fields above. The running mean of Γ is shown as a continuous blue line. The horizontal lines are the mean circulations before ($\overline{\Gamma_{\alpha=0}}$) and after ($\overline{\Gamma_{\alpha=0.82}}$) the rotation starts

4. CONCLUSION

A new device for an elastically mounted cylinder experiencing vortex-induced vibrations (VIV) with adjustable damping coefficient is presented. The change of this coefficient is simulated by coupling a DC motor whose action on the oscillating mass can be modelled as a Coulomb term. Tests conducted show that the oscillating device allows to reproduce vibration regimes ranging from low- to high-mass ratio device configurations with vibrating responses similar to that typically reported in the literature. A second DC motor is used to force the cylinder into rotary oscillation along the vertical axis to increase the cross-flow vibrations. One main advantage of the proposed solution is that is is mechanically non-intrusive. The results presented are consistent with previous studies and confirm the efficiency of rotational forcing to increase the vibration amplitude, particularly in the high reduced velocity regimes ($U^* > 7$). The addition of velocity field recordings by particle image velocimetry (PIV) allows the identification of patterns in the wake and

is an essential tool for understanding the interaction between wake and cylinder forces. The next step is to control the amplitude of the oscillations by modifying the rotary oscillation of the cylinder.